nature nanotechnology

ARTICLES

PUBLISHED ONLINE: 6 JULY 2014 | DOI: 10.1038/NNANO.2014.130

Non-invasive multimodal functional imaging of the intestine with frozen micellar naphthalocyanines

Yumiao Zhang[1,2], Mansik Jeon[1,3], Laurie J. Rich[4], Hao Hong[5], Jumin Geng[1], Yin Zhang[5], Sixiang Shi[5], Todd E. Barnhart[5], Paschalis Alexandridis[2], Jan D. Huizinga[6], Mukund Seshadri[4], Weibo Cai[5]*, Chulhong Kim[1,3]* and Jonathan F. Lovell[1,2]*

There is a need for safer and improved methods for non-invasive imaging of the gastrointestinal tract. Modalities based on X-ray radiation, magnetic resonance and ultrasound suffer from limitations with respect to safety, accessibility or lack of adequate contrast. Functional intestinal imaging of dynamic gut processes has not been practical using existing approaches. Here, we report the development of a family of nanoparticles that can withstand the harsh conditions of the stomach and intestine, avoid systemic absorption, and provide good optical contrast for photoacoustic imaging. The hydrophobicity of naphthalocyanine dyes was exploited to generate purified ~20 nm frozen micelles, which we call nanonaps, with tunable and large near-infrared absorption values (>1,000). Unlike conventional chromophores, nanonaps exhibit non-shifting spectra at ultrahigh optical densities and, following oral administration in mice, passed safely through the gastrointestinal tract. Non-invasive, non-ionizing photoacoustic techniques were used to visualize nanonap intestinal distribution with low background and remarkable resolution, and enabled real-time intestinal functional imaging with ultrasound co-registration. Positron emission tomography following seamless nanonap radiolabelling allowed complementary whole-body imaging.

In the USA alone, digestive diseases are implicated in upwards of 100 million ambulatory care visits annually[1], and improved imaging approaches could offer significant benefit. Capsule endoscopy, enteroscopy, magnetic resonance imaging, computed tomography, X-rays and ultrasound (US) are presently used for assessing gastrointestinal (GI) conditions[2]. Functional imaging of intestinal motor patterns such as peristalsis and segmentation is not usually performed due to a lack of accessible, effective and non-invasive methods. Intestinal motility dysfunction is implicated in diseases such as small bowel bacterial overgrowth[3], irritable bowel syndrome[4], inflammatory bowel disease[5] and constipation[6]. Motility disorders present serious side effects in numerous diseases including thyroid disorders[7], diabetes[8] and Parkinson's[9]. To provide appropriate treatment and to evaluate effectiveness, the existence of and nature of motor disturbances should be known, but current approaches are by trial and error. In preclinical studies, motility and peristalsis are conventionally assessed by *ex vivo* measurements. New imaging techniques that safely and non-invasively assess anatomic and functional imaging will lead to better diagnosis and treatment of gut diseases.

Photoacoustic (PA) imaging is a non-ionizing modality with deeper penetration than other optical methods[10–13]. Instrumentation costs are low and the systems are small and modular with the potential to become widely accessible for routine clinical probing of chronic and acute GI conditions. PA imaging is a data-rich, inherently real-time modality suitable for imaging dynamic intestinal processes such as peristalsis and segmentation without sacrificing spatial resolution. Additionally, PA imaging is a safe, non-invasive and non-ionizing modality, which matches the preferred characteristics of GI imaging, especially for paediatric patients[14]. PA techniques are particularly useful for imaging exogenous near-infrared (NIR, 650–1,000 nm) contrast agents[15,16]. Any luminal GI contrast agent should avoid systemic absorption into the body, because the subsequent loss of contrast agent from the intestine will lead to signal reduction, interfere with quantitative measurements and introduce toxicity concerns. Finally, the contrast agent should not degrade in the harsh chemical and digestive environments of the stomach and intestine.

Formation of frozen naphthalocyanine micelles

Chromophores of varying hydrophobicity were examined to determine whether they spontaneously assembled into stable nanoparticles following dilution into a biocompatible surfactant. Pluronic (poly(oxyethylene)-poly(oxypropylene)-poly(oxyethylene); PEO-PPO-PEO) F127 was selected because it is approved by the US Food and Drug Administration (FDA) for oral consumption[17]. To examine chromophore–F127 complex stability, the solutions were dialysed against the bile surfactant sodium cholate, which can pass through dialysis tubing because of its small micelle size. As shown in Fig. 1a, dyes that were very hydrophobic based on the octanol–water partition coefficient (log *P* values, predicted with the ALOGPS algorithm[18]) exhibited high retention after dialysis so did not readily exchange with the large excess of cholate micelles. Of the dyes evaluated, phthalocyanine (Pc) and naphthalocyanine (Nc) derivatives (Fig. 1b), which are characterized by their tetrapyrrole structure and extreme hydrophobicity, were nearly fully

[1]Department of Biomedical Engineering, University at Buffalo, State University of New York, Buffalo, New York 14260, USA, [2]Chemical and Biological Engineering, University at Buffalo, State University of New York, Buffalo, New York 14260, USA, [3]Department of Creative IT Engineering, POSTECH, Pohang, Korea, [4]Department of Pharmacology and Therapeutics, Roswell Park Cancer Institute, Buffalo, New York 14263, USA, [5]Department of Radiology and Department of Medical Physics, University of Wisconsin, Madison, Wisconsin 53705, USA, [6]Farncombe Family Digestive Health Research Institute, Department of Medicine, McMaster University, Hamilton, Ontario L8N 3Z5, Canada. *e-mail: wcai@uwhealth.org; chulhong@postech.edu; jflovell@buffalo.edu

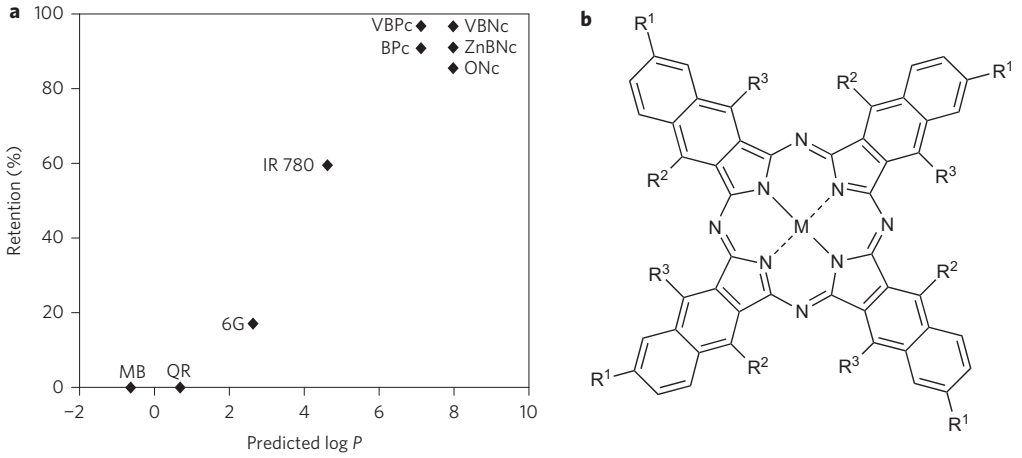

Figure 1 | Spontaneous formation of non-exchangeable F127–naphthalocyanine frozen micelles. a, Retention of dyes of varying hydrophobicity added to an aqueous solution of 10% (wt/vol.) F127 and then dialysed against 20 mM cholate for 24 h. MB, methylene blue; QR, quinaldine red; 6G, rhodamine 6G; IR780, IR780 iodide. **b**, Chemical structure of napthalocyanines used. BNc: M = 2H; R^1 = *t*-Bu; R^2,R^3 = H. VBNc: M = VO; R^1 = *t*-Bu; R^2,R^3 = H. ZnBNc: M = Zn; R^1 = *t*-Bu; R^2,R^3 = H. ONc: M = 2H; R^1 = H; R^2,R^3 = O-$(CH_2)_3CH_3$. Phthalocyanines contain single outer benzenes. BPc: M = 2H; R^1 = *t*-Bu; R^2,R^3 = H. VBPc: M = VO; R^1 = *t*-Bu; R^2 = $N(CH_3)_2$; R^3 = H.

retained. The presence of a strongly colourful supernatant after centrifugation to remove any aggregates implied the formation of soluble nanoformulated naphthalocyanines (nanonaps). The yield of nanonaps increased with increasing F127 concentrations (Supplementary Fig. 1). No sharp increase in nanonap yield was observed above the critical micelle concentration (CMC) of F127 (~1% at room temperature)[19], implying a nanonap formation mechanism unrelated to unimer–micelle equilibrium.

Because F127 has a temperature-sensitive CMC[20] we examined the effects of lowering the solution temperature to convert micelles to F127 unimers. Reducing the temperature to 4 °C did not result in any Nc aggregation, which can be explained by the formation of frozen micelles. This enabled a novel strategy for the removal of all excess F127 (Fig. 2a). As shown in Fig. 2b, centrifugal filtration removed all free F127 at 4 °C, but the process was ineffective at 25 °C, as determined using a previously reported colorimetric assay (Supplementary Fig. 2)[21]. CMC switching did not affect the self-assembly of nanonaps, which were quantitatively retained during the 4 °C washing process (Fig. 2c). All free surfactant was removed from the nanonaps with three low-temperature wash cycles, and no further change in contact angle was observed with additional washing (Supplementary Fig. 3). Unlike nanonaps, methylene blue (MB), a dye used for PA applications, was completely removed from the retentate following three centrifugal filtration washes.

The nanoparticles formed 20 nm spheres (Fig. 2d,e). Because the CMC switching process removed all excess F127, the well-dispersed nanonaps could be concentrated to high dye-to-F127 molar ratios (>3:1 dye:F127, Supplementary Table 1). We prepared 2 mg of Nc dye either in a nanonap or a liposomal formulation, using dimyristoylphosphatidylcholine (DMPC) in a 19:1 lipid:dye molar ratio. Following initial solubilization, the solutions were freeze-dried and reconstituted in a minimal volume of water (50 µl). The concentrated nanonaps dissolved in water, as shown by the extreme Nc NIR absorption of ~1,000 (Fig. 2f). After the freeze-dried liposomes were reconstituted, some Nc resolubilization was observed, but it was orders of magnitude lower than the nanonap formulation. Because CMC switching dramatically reduces the total amount of F127 surfactant present, nanonaps could be reconstituted at a much higher concentration. The phospholipid amounts required for Nc solubilization could not analogously be decreased via CMC switching, and following freeze-drying and further concentration during reconstitution, the phospholipid concentration was above the solubility limit. Difficulty in encapsulation could be further impacted by amorphous precipitation of the Nc during solvent removal.

Because nanonaps could be generated from a range of hydrophobic Pc and Nc chromophores (Fig. 1a), we set out to identify a subset with spectral properties spanning the NIR window. A range of commercially available Pc and Nc dyes were screened using the CMC switching method to generate pure nanonaps (Supplementary Fig. 4). The dye extinction coefficients ranged from 1.0×10^5 M^{-1} cm^{-1} to 2.2×10^5 M^{-1} cm^{-1} in organic solvents, whereas in the nanonap form these decreased to $0.4–1.5 \times 10^5$ M^{-1} cm^{-1} (Supplementary Table 1). This suggests that the dense arrangement of Ncs in the nanonaps led to altered electronic properties and intermolecular interactions, which was further supported by full fluorescence self-quenching of aqueous nanonaps (Supplementary Fig. 5). Powder diffraction analysis of freeze-dried samples did not reveal any crystalline Nc within the nanonaps, indicating that the dyes were probably embedded with F127 without organized stacking (Supplementary Fig. 6). It is assumed that the nanonap interior is an amorphous blend of the dyes and hydrophobic F127 PPO blocks. However, because structural studies have shown that the gyration radius of F127 PPO blocks is only 1.6 nm (ref. 22), and given the contiguous nature of PEO-PPO-PEO blocks, the interior of the nanonaps may also contain a small portion of hydrophilic PEO, which would segregate from the more hydrophobic Nc and PPO. The aqueous-facing shell of nanonaps is presumed to be composed exclusively of PEO. Further studies are required to gain deeper insight into the nanonap formation mechanism.

A total of one Pc and three Nc dyes were identified, which gave rise to nanonaps with peaks at 600, 707, 793 and 863 nm (Fig. 3a,b). The nanonaps generated absorption spanning the NIR spectrum while maintaining reasonably narrow full-width at half-maxima (50–100 nm). Because PA imaging can resolve multiple absorption wavelengths[23], multi-wavelength classes of nanoparticles are desirable[24]. The PA spectral response of the nanonaps aligned with their absorption spectra (Supplementary Fig 7). The nanoparticles could be concentrated into fully soluble solutions with absorptions greater than 1,000. One advantage of nanonaps over free dyes was that upon concentration, absorption peak positions displayed negligible shifting (Fig. 3c). This was assessed by measuring the absorption of a concentrated solution (~1,000 optical densities (OD) ml^{-1}) in a 10 µm path length and then measuring a 1,000-fold dilution of

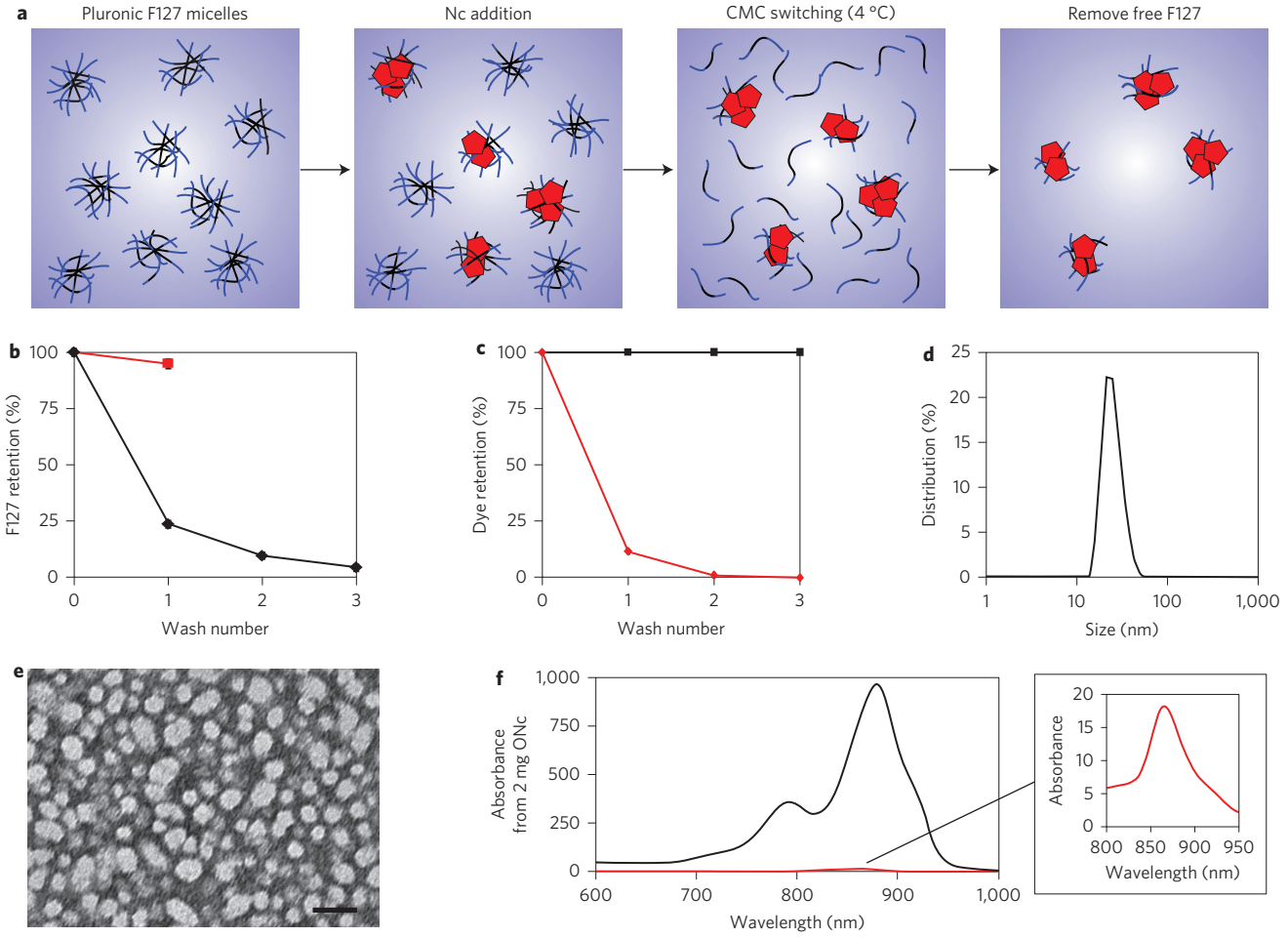

Figure 2 | Temperature-mediated CMC switching to generate surfactant-free nanonaps. a, Generation of purified nanonaps. F127 PEO blocks are in blue, PPO blocks in black and Nc dyes in red. **b**, F127 retention as a function of centrifugal filtration washes at 4 °C (black) and 25 °C (red) (mean ± s.d. for $n = 3$). **c**, F127-solubilized dye retention as a function of centrifugal filtration washes at 4 °C for Nc (black) and MB (red) (mean ± s.d. for $n = 3$). **d**, Nanonap size distribution by dynamic light scattering in water. **e**, Negative-stained transmission electron micrograph of dried nanonaps. Scale bar, 50 nm. **f**, Equivalent absorbance from concentrated, reconstituted nanonaps (black) or liposomes (red; 1:19 molar ratio of Nc:lipid) following freeze-drying of nanoparticles formed with 2 mg ONc. Inset: Magnified liposomal absorbance.

the same solution in a 1 cm path length. The commonly used PA dyes MB and indocyanine green exhibited large absorption shifts in concentrated solutions as a result of the modulated electronic properties induced by the self-interaction encountered at high concentrations. On the other hand, Ncs co-assembled with F127 in the nanonap matrix exhibited no modified peak absorption shifts, demonstrating that nanonaps prevented the concentration-dependent dye interaction that would otherwise affect absorption at higher concentrations. Although concentration-dependent absorption shifts can be useful in PA imaging[25], concentration-independent optical parameters lead to simplified analysis of contrast movement, as would be the case for GI photoacoustic tomography (PAT). Based on zeta potential measurements, nanonaps maintained a nearly neutral surface charge over a broad range of pH values (Supplementary Fig. 8).

Absorbance, as measured on a spectrophotometer, includes effects of both absorption and scattering. However, only absorption contributes to the PA effect. Resonance light scattering was used to estimate scattering. Compared with extinction-matched gold nanorods, nanonaps exhibited negligible scattering (Supplementary Fig. 9). This is in accordance with previous reports of tetrapyrrole-based nanoparticle scattering[26]. Because the reference nanorods had a low scattering-to-absorption ratio (<10%)[27], nanonaps were considered to have no scattering component. Based on the molar ratio of Nc to F127 in the purified nanonaps, and geometric calculations, we estimated that each 5,9,14,18,23,27,32,36-octabutoxy-2,3-naphthalocyanine (ONc) nanonap contains 501 molecules of Nc and 155 molecules of F127, with an optical cross-section of 2.9×10^{-17} m^2. Additional optical parameters are reported in Supplementary Table 1. Although this cross-section is two orders of magnitude lower than that of the nanorods, the unique dispersibility of the nanonaps enables them to be concentrated to orders of magnitude higher particle density while maintaining solubility. As a result, stable nanoparticle solutions are achievable with overall absorptions greater than 1,000.

Photoacoustic gut imaging

To assess the suitability of nanonaps for use as an orally administered PA agent, we determined whether nanonaps could withstand the harsh conditions of the stomach and intestine, which often pose hurdles for nanoparticles[28]. When nanonaps were dialysed in simulated gastric fluid (SGF) or simulated intestinal fluid (SIF) at 37 °C, no appreciable loss of absorption was observed, demonstrating stability under harsh dialysis conditions (Fig. 4a). In contrast, wavelength-matched gold nanoparticles stabilized by either residual cetrimonium bromide (CTAB) or by thiolated polyethylene glycol

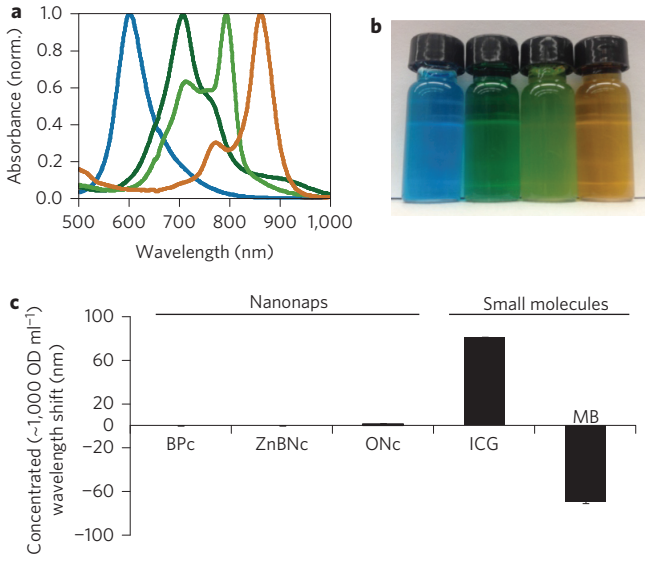

Figure 3 | Multispectral nanonaps without peak wavelength shifting at ultrahigh optical densities. a, Normalized absorbance of nanonaps formed from BPc (blue), ZnBNc (dark green), BNc (light green) or ONc (bronze). **b**, Photograph of nanonaps in water. From left to right: BPc, ZnBNc, BNc and ONc. **c**, Absorption peak wavelength shift at high optical densities. Concentrated solutions were measured in a cuvette with a path length of 10 μm and compared with a 1,000-fold dilution in water. Indicated nanonaps are compared with indocyanine green (ICG) and MB. Mean ± s.d. for $n = 3$.

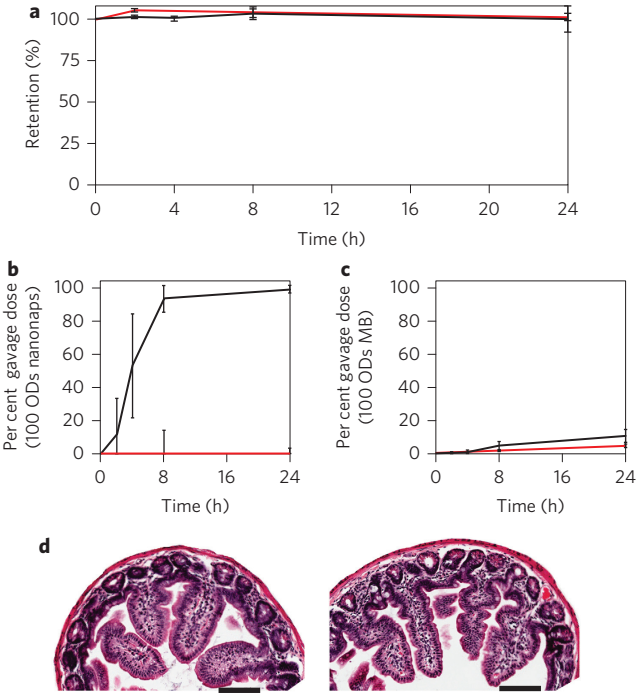

Figure 4 | Nanonaps pass safely through the intestine following oral administration. a, Retention of ONc nanonaps dialysed in simulated gastric fluid (red) or simulated intestinal fluid (black) at 37 °C (mean ± s.d. for $n = 3$). **b**, Excretion of 100 ODs of ONc nanonaps in faeces (black) and urine (red) (mean ± s.d. for $n = 3$ mice). **c**, Excretion of 100 ODs of MB in faeces (black) and urine (red) (mean ± s.d. for $n = 3$ mice). **d**, Haematoxylin and eosin-stained intestine section of a control mouse (left) or a mouse 24 h after gavage of 100 ODs of ONc nanonaps (right). Villi and crypts were intact without influx of inflammatory cells. Scale bars, 100 μm.

(PEG) did not withstand the same dialysis conditions and aggregated rapidly (Supplementary Fig. 10). In water, 1.2 mg ml^{-1} ONc nanonaps generated over 100-fold greater PA signal than concentration-matched and wavelength-matched gold nanorods (Supplementary Fig. 11). Semiconducting organic nanoparticles have also been reported to generate more PA contrast than gold at matching mass concentrations[29].

The cellular toxicity of ONc nanonaps was assessed using Caco-2 cells. Whereas MB induced toxicity when incubated in cell media with absorbance greater than 1, nanonaps did not exhibit any toxicity up to an absorbance of 100, the highest value tested (Supplementary Fig. 12). Encouraged by these results, we administered 100 ODs of ONc nanonaps via gavage to mice. Nanonaps were completely excreted in the faeces (Fig. 4b). The lack of intestinal absorption probably stemmed from both the 20 nm size of the nanonaps (which prevents passive diffusion through membranes) and the PEO character of F127 (which prevents bioadsorption)[30]. For comparison, 100 ODs of MB was administered in the same manner. MB was systemically absorbed and was detectable in urine, with most of the MB remaining in the body or being metabolized (Fig. 4c).

The effect of nanonaps on intestinal tissues was examined using histology (Fig. 4d). No noticeable inflammatory response or damaging effects were induced, and the intestinal villi and crypts appeared healthy. Given the safety of nanonaps predicted by their quantitative excretion and lack of systemic absorption, we next assessed the acute toxicity of nanonaps using an oral dose of 50,000 OD_{860} kg^{-1}. This represents a tenfold excess of the functional nanonap dose used for imaging applications. There were no adverse behavioural or weight changes in male or female mice over the two-week study (Supplementary Fig. 13a). Histology revealed no systemic (Supplementary Fig. 13b) or gastrointestinal (Supplementary Fig. 13c) toxicity.

We next examined the utility of nanonaps for non-invasive PAT of the intestine *in vivo*. As shown in Fig. 5a, PA imaging using a custom-built single-element scanning system revealed the biodistribution of nanonaps in the GI tract with an axial resolution of 100 μm. Progression of zinc-2,11,20,29-tetra-*tert*-butyl-2,3-naphthalocyanine (ZnBNc) nanonaps through the intestine was clearly observed. Negligible background was detected, enabling the clear resolution of intestinal features; indeed, individual small bowel diverticula were distinguishable. Depth encoding analysis revealed further spatial details of intestinal distribution with depth mapping to 5 mm (Fig. 5b). Strong isoflurane anaesthetization (3% vol/vol) halted intestinal motility (Supplementary Fig. 14). This was fortuitous, because each high-resolution, whole-abdomen scan took 30 min or longer to perform. Although lower resolution and smaller scanning areas would reduce scan times, single-element transducer approaches are not ideal for data-rich functional imaging of dynamic intestinal processes.

For dynamic imaging, a Vevo LAZR transducer array system was used. A total of 100 ODs of ONc nanonaps were administered via gavage. As shown in the transverse slice in Fig. 5c, PA (colour) overlaid perfectly with US (grey) to reveal the nanonap distribution in the intestine below the abdomen surface, with minimal background. The five frames per second scanning speed enabled detailed tracking of nanonap movement in the intestine. Rapid changes in nanonap flow were readily apparent (Fig. 5d) and detailed peristaltic movements were clear (Supplementary Movie 1). By selecting a region of interest that displayed undulating nanonap content, segmentation or peristaltic flow was quantified. The flow of nanonaps into a representative region of interest occurred periodically with distinct inflow and outflow movements (Fig. 5e). Calculation of the rate of peristaltic intestinal flow shown in Fig. 5f demonstrated contractions close to 30 per minute, which is consistent with values reported in mice[31].

By examining US co-registration, intestinal nanonap distribution was mapped to anatomical features. As shown in Fig. 5g, the bladder

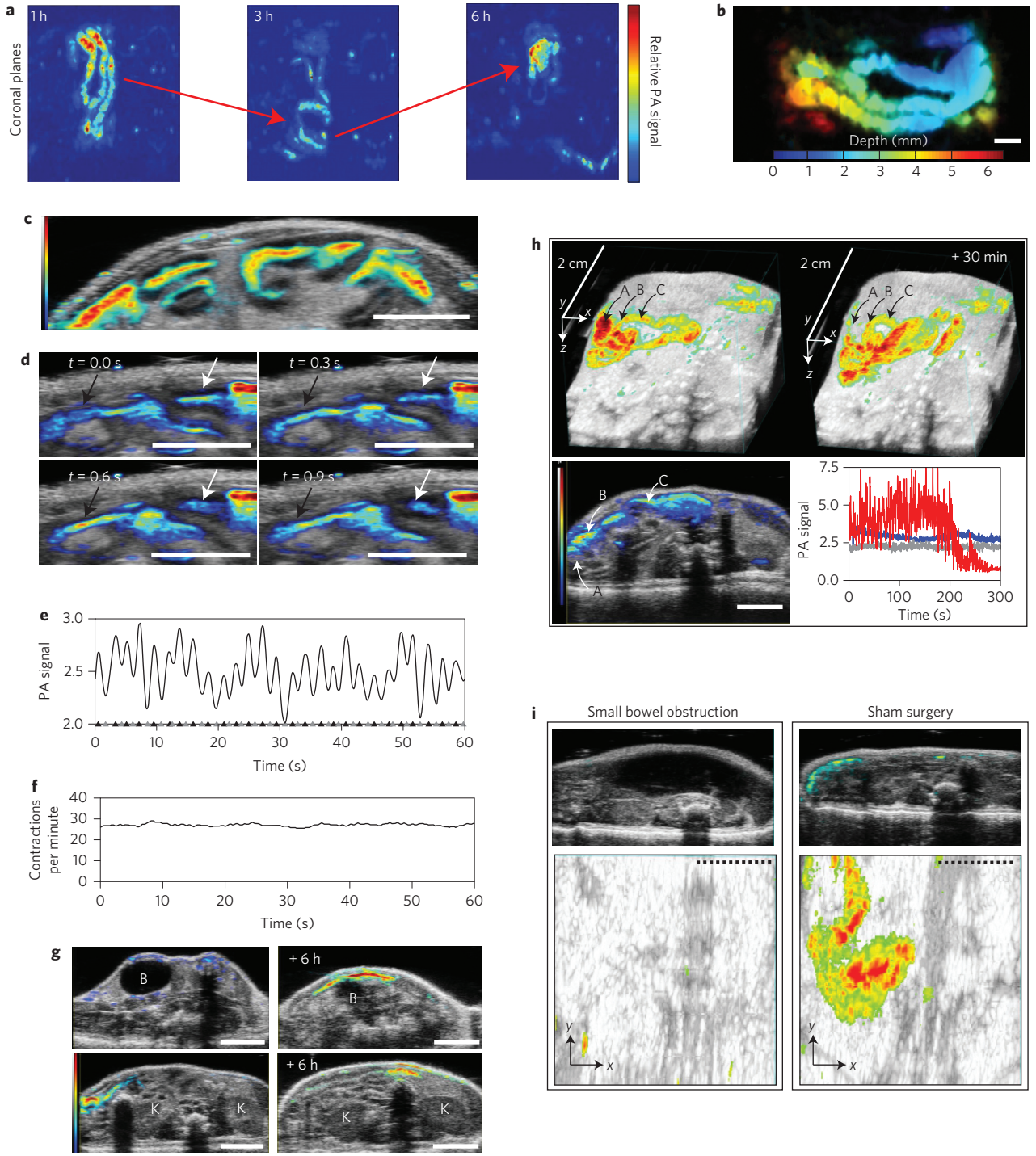

Figure 5 | Non-invasive anatomical and functional PA imaging of the intestine using nanonaps. a, PA MIP of nanonaps following gavage of 100 ODs of ZnBNc nanonaps using a single-transducer PA system. Red arrows show nanonap transit. **b**, Depth-encoded PA MIP of the intestine visualizing ZnBNc nanonaps. **c**, Real-time multimodal mouse intestinal transverse plane with PA signal (colour) and simultaneous US (grey) acquisition following gavage of 100 ODs of ONc nanonaps. **d**, Nanonap movement in the intestine. Black arrow shows inflow and white arrow shows outflow. **e**, Intestinal region-of-interest analysis. First-derivative zero crossings provide the time of maximal nanonap inflow (black triangles) and outflow (grey triangles) points. **f**, Rate of contractile motion from the region, plotted over time. **g**, Co-registered US for anatomical mapping of nanonaps. The bladder (B) and kidneys (K) are located with US (grey), and the nanonap PA signal is shown in colour. **h**, US (grey)/PA(colour) MIPs of transverse slices, showing ONc nanonap intestinal transit over time. The MIP was used to orient the PA signal within a single slice of interest (lower left). Outflow quantification over time of nanonaps in area A (red) shown with reference to two others that maintained steady nanonap content in areas B (blue) and C (grey). The fluctuations in A are due to contractile inflow and outflow of nanonaps. **i**, US/PA detection of intestinal obstruction. Mice were subjected to duodenal ligations or sham surgery. 100 ODs of ONc nanonaps were administered and mice were imaged 1 h later. The top images show a transverse slice 2.4 cm above the bladder, showing the swollen stomach in the obstructed mice. The bottom images show US/PA MIPs. An unobstructed flow of nanonaps is clear in the sham group. The dashed line indicates the approximate surgical incision site and the image width corresponds to 2.4 cm. Representative images for $n = 3$ per group. All scale bars, 5 mm.

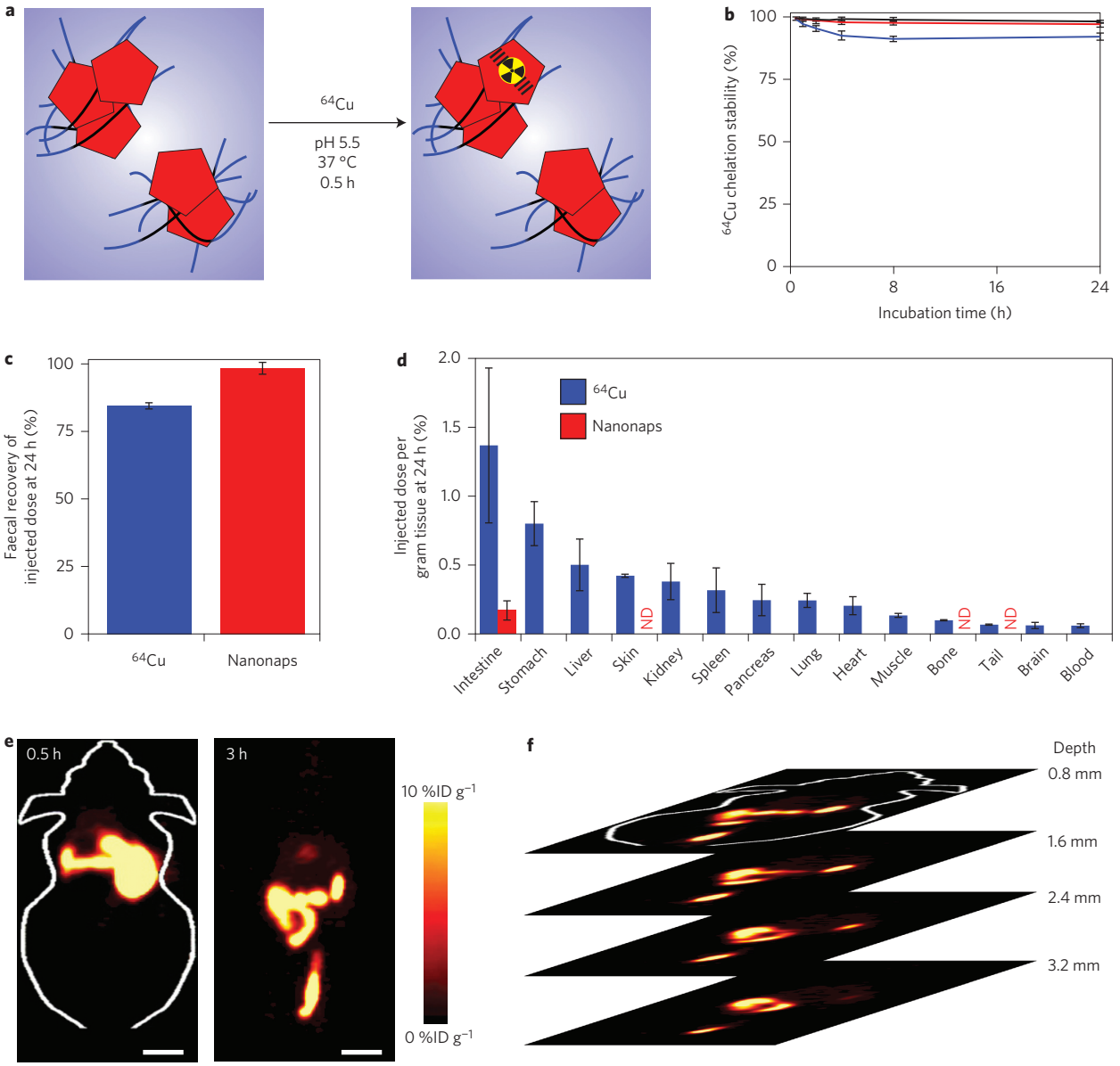

Figure 6 | Seamless nanonap labelling with ^{64}Cu for whole-body PET imaging of the GI tract. a, Nanonap labelling using ^{64}Cu. F127 PEO blocks are shown in blue, PPO blocks in black, Nc dyes in red and ^{64}Cu is shown as the radioactive yellow circle. **b**, Retention stability of ^{64}Cu chelation in radiolabelled nanonaps in simulated gastric fluid (red), simulated intestinal fluid (blue) and water (black) incubated at 37 °C (mean ± s.d. for $n = 3$). **c**, Faecal clearance of ONc nanonaps and chelated ^{64}Cu in mice 24 h after gavage of 100 ODs of ONc nanonaps. ^{64}Cu was assessed using gamma counting and nanonaps using absorption. (Mean ± s.d. for $n = 3$–4 mice.) **d**, Biodistribution of ^{64}Cu and nanonaps 24 h after gavage. No data (ND) were obtained for some samples because they were not measured. (Mean ± s.d. for $n = 3$–4 mice.) **e**, Representative PET imaging of nanonaps. 100 ODs of ^{64}Cu-labelled ONc nanonaps were gavaged and mice were imaged at the indicated time points. Scale bars, 1 cm. **f**, Representative 0.8-mm-thick coronal slices through the mouse, 3 h after gavage.

and kidneys were identified with US and the relative position of adjacent intestinal nanonaps changed over time. Two US/PA maximum intensity projections (MIPs) were generated from a stack of scans that traced the movement of nanonaps through the intestine over a 30 minute period (Fig. 5h). The MIP is useful for providing the intestinal orientation in any given individual transverse slice. The indicated regions of interest showed, in real time, the out-of-plane passing of nanonaps through a transverse slice of the intestine. Compared to control regions B and C, which contain relatively constant nanonap volumes, nanonaps quantitatively exited from region A over one minute and demonstrated peristaltic contractions in the process.

Small bowel obstructions require 300,000 operations annually in the USA[32]. To determine whether US/PA imaging could be useful for detecting intestinal obstructions, we used a surgically induced duodenal ligation mouse model[32]. Following duodenal ligation or sham treatment (opening the abdomen but omitting the ligation), the abdomen was sutured closed. The mice were then administered a 100 OD_{860} dose of ONc nanonaps and imaged 1 h post-gavage. The stomachs of the mice with obstructions visibly swelled to a large volume. US transverse slices showed a prominent void stomach volume in the ligated mice, but not in the sham-treated mice (Fig. 5i, top). Although US could distinguish the bloated stomach of the obstructed mice, the PA signal was barely detectable. The enlarged stomachs of the obstructed mice contained large pockets of air that may have caused PA attenuation, and further investigation of this phenomenon is required. In the obstructed mice, barely any PA signal was detected over the entire intestinal

area (Fig 5i, bottom). However, sham-treated mice displayed a strong PA signal, demonstrating that nanonaps progressed uninhibited through the intestine. Thus, nanonaps may be useful as a diagnostic tool for the detection of small bowel obstructions.

Based on their high absorption, both ZnBNc (707 nm) and ONc nanonaps (860 nm) were suitable for low-background GI PA imaging. The selection of optimal nanonap wavelength is case-dependent. For example, many tunable lasers currently used in PA instrumentation generate a higher laser output at 707 nm, whereas 860 nm may have less intrinsic biological background and scattering. In chicken breast tissue, absorbance-matched ONc and ZnBNc nanonaps could both be detected easily up to a depth of 2.5 cm, with similar PA signal-to-noise ratios (Supplementary Fig. 15). The pulse energies used were only 2 and 1.5 mJ cm^{-2}, corresponding to only ~1/10 and ~1/30 of the laser safety limits for ZnBNc and ONc nanonap wavelengths, respectively.

Positron emission tomography

Although PA technology is improving rapidly, deep tissue (>5 cm) PA imaging is yet to be reported in humans. Because positron emission tomography (PET) is clinically used for non-invasive whole-body imaging, we examined nanonap-based PET imaging as a complementary technique. The four pyrrole nitrogens within the Nc macrocycle can coordinate with copper to serve as a chelator[33] and it has been shown that the positron emitter ^{64}Cu can be used to conveniently label intact tetrapyrrole-based nanoparticles[34]. Because nanonaps are formed from Ncs themselves, no additional steps of chelator conjugation are required.

When nanonaps were incubated with ^{64}Cu in aqueous solution, labelling was achieved in just 30 minutes with over 65% radiolabelling yield (Fig. 6a and Supplementary Table 2). Size and zeta potential were unaffected (Supplementary Fig. 16). Following the removal of free copper, when ^{64}Cu-nanonaps were incubated in SIF and SGF at 37 °C, the chelation was stable *in vitro* (Fig. 6b). A 100 OD_{860} dose of radiolabelled ONc nanonaps was then gavaged (7.4 MBq per mouse). Gamma counting validated that faecal clearance of ^{64}Cu-nanonaps followed the same kinetics as the unlabelled ones (Supplementary Fig. 17). In total, 99% of nanonaps were excreted in faeces, compared with 85% of the ^{64}Cu radiolabel (Fig. 6c). This discrepancy was probably due to the displacement of some of the copper from the Nc chelate in the harsh GI environment. Minimal radioactivity remained in any part of the mouse, with all organs retaining less than 1.5% ID g^{-1} of ^{64}Cu (Fig. 6d). Because they were cleared in faeces, nanonaps themselves were not detected in any organs, except for a small trace amount remaining in the intestine.

PET was used to follow the movement of nanonaps through the GI tract. Radioactivity was present in the stomach and upper intestine after oral gavage, as can be seen from the PET images at 0.5 h (Fig. 6e). A clear distribution pattern of ^{64}Cu-nanonaps in the intestine was observed 3 h after administration. Because PET is tomographic with no tissue penetration limits, serial whole-body consecutive coronal slices of the mouse could be obtained (Fig. 6f). Tomographic analysis revealed background-free intestinal visualization in three dimensions (Supplementary Movie 2).

Conclusions

Owing to the high Nc hydrophobicity, kinetically frozen nanonaps could be formed that are stable in the gut, avoid systemic absorption, and give rise to extreme and tunable optical absorption in the NIR. They are organic, assembled from an FDA-approved surfactant, and are completely excreted in faeces without observed toxicity. Real-time US/PA gut imaging using nanonaps provided high-resolution, low-background, real-time, proof-of-principle mapping of intestinal anatomy, pathology and function. The direct use of nanonaps for PET will enable quantitative, sensitive, clinically established imaging approaches with full tissue penetration for whole-body imaging. The spatial resolution limitations of PET (a few millimetres) can be compensated with localized PAT techniques using a single agent. In applications beyond GI imaging, nanonaps, because of their multimodal nature, stability and small size above the renal clearance threshold, also hold potential for use as an intravenously administered contrast agent. Future directions of research may include modifying nanonap surface properties for targeted detection and examining multi-colour PA imaging for diagnosis of gut diseases.

Methods

See Supplementary Information for full methods. Materials were purchased from Sigma unless otherwise noted.

Nanonap formation. Log *P* values were evaluated using the ALOGPS 2.1 algorithm. Dyes (2 mg) were dissolved in organic solvent and added to 10 ml Pluronic F127 (10% wt/vol) and stirred until organic solvent evaporation. After centrifugation to remove aggregates, 100 µl of the supernatant was diluted in 3 ml of 20 mM sodium cholate and dialysed for 24 h against 20 mM sodium cholate. Retention was based on absorbance. For nanonap formation, 2 mg of dye was dissolved in 1 ml dichloromethane and added to an F127 solution as above. To remove unincorporated F127 via CMC switching, the clarified solution was cooled on ice and subjected to centrifugal filtration (Fisher #UFC9-100-24) at 4 °C until 200 µl of solution was retained. Water was added back to the concentrate and the washing procedure was repeated three times.

Nanonap physical and optical properties. Size and zeta potential measurement were carried out with dynamic light scattering using a Nano ZS90 Zetasizer (Malvern Instruments). Transmission electron microscopy was performed using a JEM-2010 electron microscope with 1% uranyl acetate staining. Absorbance was measured with a Lambda 35 UV/VIS spectrophotometer (Perkin Elmer) using cuvettes with 1 cm path lengths, except for the high-concentration spectral shifting analysis, which used cuvettes with 10 µm path lengths. X-ray diffraction analysis was carried with freeze-dried samples on a Rigaku Ultima IV. Scattering and fluorescence properties were assessed using a spectrofluorometer (Photon Technology International).

To assess the stability of the nanonaps in SGF and SIF, concentrated nanonaps were diluted into the fluids so that the absorbance was close to 1, then dialysed at 37°C against SGF (Ricca, #7108-32) with added pepsin and pancreatin-containing SIF (Ricca #7109-32). CTAB (860 nm) stabilized gold nanorods and 850 nm thiol-PEG-stabilized gold nanorods (NanoRods LLC, #C122-CTAB and C120-PEG) were dialysed in the same manner.

Nanonap clearance and toxicity. Animal experiments were performed in accordance with the University at Buffalo Institutional Animal Care and Use Committee. Six-week female BALB/c mice (Harlan) were held without food overnight with free access to water. After gavaging 100 ODs of ONc nanonaps or MB, mice were transferred to metabolic cages, and faeces and urine were collected separately. For the determination of recovery, the absorbance of urine or serum samples was measured directly. Tissues or faeces were dissolved in 2 ml of organic solvent and were disrupted until the dyes were dissolved completely, and absorbance was assessed. For acute toxicity, 6-week-old male and female BALB/c mice were gavaged 1,000 OD_{860} of ONc nanonaps per 20 g or kept as controls ($n = 5$ per group). Behaviour was monitored and mass was measured weekly. After two weeks, mice were killed and organs were harvested. Organs were immersed in formalin (VWR #16004-114) before sectioning and haematoxylin and eosin staining.

PA experiments. A custom-built, reflection-mode single-element transducer PAT system was used for high-resolution scanning imaging. A Vevo LAZR US/PA system was used for real-time imaging. The movement of nanonaps in the digestive system was monitored after gavage of 100 ODs of the indicated nanonaps in female BALB/c mice. Region-of-interest analysis was performed with the system software. The rate of peristalsis was determined by derivative analysis of region-of-interest intensity. For intestinal obstruction, 12–14 g female CD-1 mice (Harlan) were used, with $n = 3$ per group. The abdomen was opened with a 1 cm transverse incision near the stomach and the duodenum was ligated with nylon sutures (VWR #89219-096). Sham-treated mice had no duodenum ligation performed, but otherwise it was an identical procedure. The abdomen skin was sutured closed again and, within a few hours, mice were administered a 100 OD_{860} dose of ONc nanonaps by gavage. One hour later, the mice were anaesthetized and imaged with the Vevo LAZR system.

Radiolabelling experiments. For labelling, 37 MBq of $^{64}CuCl_2$ was diluted in 300 µl of 0.1 M sodium acetate (pH 5.5) and added to 400 OD_{860} ONc nanonaps for 30 min at 37 °C. The ^{64}Cu-nanonaps were purified by centrifugal filtration and resuspended in 500 µl of PBS for further use. For *in vitro* stability, one OD_{860} of ^{64}Cu-nanonaps was resuspended in 1 ml of SGF or SIF and incubated at 37 °C with stirring. Portions of the mixture (50 µl) were sampled at different time points and

washed by centrifugal filtration for analysis. Radioactivity was measured by a Wizard2 gamma counter (Perkin Elmer).

PET scans were performed using an Inveon microPET/microCT rodent model scanner (Siemens). After overnight fasting, each BALB/c mouse was gavaged ~7.4 MBq of ^{64}Cu-nanonaps (100 OD_{860}). Static PET scans (5–10 min) were performed at various time points post-injection. Images were reconstructed using a maximum *a posteriori* algorithm without scatter correction. After 24 h, mice were killed and biodistribution was measured with gamma counting.

Received 17 May 2013; accepted 2 June 2014; published online 6 July 2014

References

1. Everhart, J. E. & Ruhl, C. E. Burden of digestive diseases in the United States part I: overall and upper gastrointestinal diseases. *Gastroenterology* **136,** 376–386 (2009).
2. Dye, C. E., Gaffney, R. R., Dykes, T. M. & Moyer, M. T. Endoscopic and radiographic evaluation of the small bowel in 2012. *Am. J. Med.* **125,** 1228.e1–1228.e12 (2012).
3. Husebye, E. Gastrointestinal motility disorders and bacterial overgrowth. *J. Intern. Med.* **237,** 419–427 (1995).
4. Soffer, E. E. Small bowel motility: ready for prime time? *Curr. Gastroenterol. Rep.* **2,** 364–369 (2000).
5. Bassotti, G. *et al.* Gastrointestinal motility disorders in inflammatory bowel diseases. *World J. Gastroenterol.* **20,** 37–44 (2014).
6. Lembo, A. & Camilleri, M. Chronic constipation. *N. Engl. J. Med.* **349,** 1360–1368 (2003).
7. Shafer, R. B., Prentiss, R. A. & Bond, J. H. Gastrointestinal transit in thyroid disease. *Gastroenterology* **86,** 852–855 (1984).
8. Abrahamsson, H. Gastrointestinal motility disorders in patients with diabetes mellitus. *J. Intern. Med.* **237,** 403–409 (1995).
9. Jost, W. H. Gastrointestinal motility problems in patients with Parkinson's disease. *Drugs Aging* **10,** 249–258 (1997).
10. Kim, C., Favazza, C. & Wang, L. V. *In vivo* photoacoustic tomography of chemicals: high-resolution functional and molecular optical imaging at new depths. *Chem. Rev.* **110,** 2756–2782 (2010).
11. Ke, H., Erpelding, T. N., Jankovic, L., Liu, C. & Wang, L. V. Performance characterization of an integrated ultrasound, photoacoustic, and thermoacoustic imaging system. *J. Biomed. Opt.* **17,** 056010 (2012).
12. Ntziachristos, V., Ripoll, J., Wang, L. V. & Weissleder, R. Looking and listening to light: the evolution of whole-body photonic imaging. *Nature Biotechnol.* **23,** 313–320 (2005).
13. Emelianov, S. Y., Li, P. C. & O'Donnell, M. Photoacoustics for molecular imaging and therapy. *Phys. Today* **62,** 34–39 (May, 2009).
14. Stuart, S. *et al.* The smaller bowel: imaging the small bowel in paediatric Crohn's disease. *Postgrad. Med. J.* **87,** 288–297 (2011).
15. Luke, G. P., Yeager, D. & Emelianov, S. Y. Biomedical applications of photoacoustic imaging with exogenous contrast agents. *Ann. Biomed. Eng.* **40,** 422–437 (2012).
16. De la Zerda, A., Kim, J. W., Galanzha, E. I., Gambhir, S. S. & Zharov, V. P. Advanced contrast nanoagents for photoacoustic molecular imaging, cytometry, blood test and photothermal theranostics. *Contrast Media Mol. Imaging* **6,** 346–369 (2011).
17. Zhang, W. *et al.* Synthesis and characterization of thermally responsive pluronic F127–chitosan nanocapsules for controlled release and intracellular delivery of small molecules. *ACS Nano* **4,** 6747–6759 (2010).
18. Tetko, I. V. & Tanchuk, V. Y. Application of associative neural networks for prediction of lipophilicity in ALOGPS 2.1 program. *J. Chem. Inf. Comput. Sci.* **42,** 1136–1145 (2002).
19. Lin, Y. & Alexandridis, P. Temperature-dependent adsorption of pluronic F127 block copolymers onto carbon black particles dispersed in aqueous media. *J. Phys. Chem. B* **106,** 10834–10844 (2002).
20. Chandaroy, P., Sen, A., Alexandridis, P. & Hui, S. W. Utilizing temperature-sensitive association of pluronic F-127 with lipid bilayers to control liposome-cell adhesion. *Biochim. Biophys. Acta Biomembr.* **1559,** 32–42 (2002).
21. Ahmed, F., Alexandridis, P. & Neelamegham, S. Synthesis and application of fluorescein-labeled pluronic block copolymers to the study of polymer–surface interactions. *Langmuir* **17,** 537–546 (2001).
22. Phipps, J. S., Richardson, R. M., Cosgrove, T. & Eaglesham, A. Neutron reflection studies of copolymers at the hexane/water interface. *Langmuir* **9,** 3530–3537 (1993).
23. Mallidi, S. *et al.* Multiwavelength photoacoustic imaging and plasmon resonance coupling of gold nanoparticles for selective detection of cancer. *Nano Lett.* **9,** 2825–2831 (2009).
24. De la Zerda, A. *et al.* Family of enhanced photoacoustic imaging agents for high-sensitivity and multiplexing studies in living mice. *ACS Nano* **6,** 4694–4701 (2012).
25. Bayer, C. L., Nam, S. Y., Chen, Y. S. & Emelianov, S. Y. Photoacoustic signal amplification through plasmonic nanoparticle aggregation. *J. Biomed. Opt.* **18,** 016001 (2013).
26. Lovell, J. F. *et al.* Porphysome nanovesicles generated by porphyrin bilayers for use as multimodal biophotonic contrast agents. *Nature Mater.* **10,** 324–332 (2011).
27. Jain, P. K., Lee, K. S., El-Sayed, I. H. & El-Sayed, M. A. Calculated absorption and scattering properties of gold nanoparticles of different size, shape, and composition: applications in biological imaging and biomedicine. *J. Phys. Chem. B* **110,** 7238–7248 (2006).
28. Carino, G. P. & Mathiowitz, E. Oral insulin delivery. *Adv. Drug Deliv. Rev.* **35,** 249–257 (1999).
29. Pu, K. *et al.* Semiconducting polymer nanoparticles as photoacoustic molecular imaging probes in living mice. *Nature Nanotech.* **9,** 233–239 (2014).
30. Malmsten, M., Emoto, K. & Van Alstine, J. M. Effect of chain density on inhibition of protein adsorption by poly(ethylene glycol) based coatings. *J. Colloid Interface Sci.* **202,** 507–517 (1998).
31. Kwon, S. & Sevick-Muraca, E. M. Non-invasive, dynamic imaging of murine intestinal motility. *Neurogastroenterol. Motil.* **23,** 881–e344 (2011).
32. Gittes, G. K., Nelson, M. T., Debas, H. T. & Mulvihill, S. J. Improvement in survival of mice with proximal small bowel obstruction treated with octreotide. *Am. J. Surg.* **163,** 231–233 (1992).
33. Ali, H. & van Lier, J. E. Metal complexes as photo- and radiosensitizers. *Chem. Rev.* **99,** 2379–2450 (1999).
34. Liu, T. W., MacDonald, T. D., Shi, J., Wilson, B. C. & Zheng, G. Intrinsically copper-64-labeled organic nanoparticles as radiotracers. *Angew. Chem. Int. Ed.* **51,** 13128–13131 (2012).

Acknowledgements

The authors thank L.L. Balos for assistance with histology, C. Cheng for assistance with dynamic light scattering measurements, and E. Huynh and G. Zheng for assistance with photoacoustic spectroscopy. This work was supported by the National Institutes of Health (W.C., R01CA169365; J.F.L., DP5OD017898; M.S., S10OD010393), the Department of Defense (W.C., W81XWH-11-1-0644), the Korean Ministry of Science, ICT and Future Planning (IT Consilience Creative Program; C.K. and J.F.L., NIPA-2013-H0203-13-1001; C.K., NRF-2011-0030075) and a SUNY Research Foundation Collaboration Fund grant.

Author contributions

Yu.Z. and J.F.L. conceived the project. Yu.Z, M.J., L.J.R., H.H. and J.G. were responsible for most data collection. Yu.Z., P.A. and J.F.L. planned experiments and interpreted the data related to nanonap formulation. H.H., Yi.Z., S.S., T.E.B. and W.C. planned experiments and interpreted the data related to nanonap radiolabelling. Yu.Z., M.J., L.J.R., J.D.H., M.S., C.K. and J.F.L. planned experiments and interpreted the data related to photoacoustic imaging. Yu.Z., J.G. and J.F.L. planned toxicity studies and interpreted the data. Yu.Z., M.J., H.H., J.D.H., W.C., C.K. and J.F.L. wrote the manuscript.

Additional information

Supplementary information is available in the online version of the paper. Reprints and permissions information is available online at www.nature.com/reprints. Correspondence and requests for materials should be addressed to W.C., C.K. and J.F.L.

Competing financial interests

The authors declare no competing financial interests.